

# Evolution of Sliver Defect in Ni-Based Single Crystal Superalloy



YAQI HUANG, JIAN SHEN, DONG WANG, GUANG XIE, YUZHANG LU,  
LANGHONG LOU, and JIAN ZHANG

The evolution of sliver defect in a Ni-based single crystal superalloy was explored by casting samples with a similar geometry of the airfoil section of a turbine blade using optical microscope and electron backscattered diffraction. It was found that the sliver generally initiated from 1 to 2 tertiary dendrites at the diverging boundary between the mold wall and matrix. All slivers were tilt from matrix along the [001] and some of them rotated relative to the matrix on the plane perpendicular to the solidification direction. During solidification sliver in most castings grew with a fixed orientation. All slivers can extend along the solidification direction to the top of the casting. Most of the sliver defects showed constant width and did not extend on the casting surface. However, the sliver with large misorientation to matrix on the cross section perpendicular to the solidification direction extended on the casting surface and into the casting quickly.

<https://doi.org/10.1007/s11661-020-06003-9>

© The Minerals, Metals & Materials Society and ASM International 2020

## I. INTRODUCTION

NI-BASED single crystal (SX) superalloy is widely applied in the hot section of advanced aero-engine and gas turbines due to the excellent mechanical performance at elevated temperature.<sup>[1,2]</sup> With the increasing content of the refractory elements in SX alloy and the complexity in geometry of the blade, the occurrence of casting defects in SX blade, such as stray grains,<sup>[3,4]</sup> freckle,<sup>[5,6]</sup> low angle boundary<sup>[7,8]</sup> and sliver References 9 through 11 becomes rather frequent during directional solidification (DS). However, compared with other defects, sliver defect is less well understood in the past.

Sliver is observed as strip-like contrast in SX and belongs to the low to medium angle misorientation defects.<sup>[10]</sup> It has been reported that tensile properties and creep rupture lives decreased with the increase of misorientation angle of a low angle grain boundary in SX superalloys.<sup>[12,13]</sup> One would also expect that sliver defect reduces the properties as it has similar structure to that of the low angle grain boundary, although no information has been reported so far in the open

literature. Therefore, it is important to understand the initiation and evolution of this defect in SX castings.

It is generally accepted that the initiation of sliver is related to the dendrite deformation in mushy zone References 9 through 11. Researcher studied the sliver generated from the narrow channel on the top of the seed in SX casting and found that high stresses in the constricted channel induced the sliver defects. The dendrites were loaded with both bending moments and torques owing to different thermal contraction between mold and metal.<sup>[10]</sup> Furthermore, the formation of lateral sliver defects on the platform was also examined by Sun *et al.*<sup>[9]</sup> It is concluded that the defects generated due to the high contraction stresses around the connections of platform and the SX body. Recently, detailed X-ray computed tomography (XCT) and electron backscattered diffraction (EBSD) characterization revealed that the origin of sliver was attributed to the localized deformation of 1 to 2 dendrites at the diverging boundary near the mold wall and thermal contraction force played an important role in sliver formation.<sup>[11]</sup>

Unfortunately, the evolution of sliver defect after its formation is still not well understood except that sliver can extend along the casting axis (parallel to DS direction) after formation.<sup>[10,11]</sup> The change of orientation and competitive growth between sliver and matrix dendrites have not been characterized. In this work, the optical microscope (OM) and EBSD were used for the metallography observation and orientation measurement. Special emphasis of the investigation was placed on the detailed characterization of the growth of sliver

YAQI HUANG is with the Superalloys Division, Institute of Metal Research, Chinese Academy of Sciences, Shenyang 110016, P.R. China and also with the School of Materials Science and Engineering, University of Science and Technology of China, Hefei 230026, P.R. China. JIAN SHEN, DONG WANG, GUANG XIE, YUZHANG LU, LANGHONG LOU, and JIAN ZHANG are with the Superalloys Division, Institute of Metal Research, Chinese Academy of Sciences. Contact e-mail: jianzhang@imr.ac.cn

Manuscript submitted January 19, 2020.

Article published online September 25, 2020

defect, as well as the orientation evolution and dendrite branching behavior.

## II. EXPERIMENTS

### A. SX Casting

SX superalloy PWA 1483 was used in the experiments and the nominal composition of the alloy is listed in Table I. The SX casting used in the experiments can be referred to the Figure 1(a) in Reference 11, which exhibited a similar geometry of the airfoil section of a turbine blade. The cross section of the casting gradually increased from bottom to top. Spiral grain selector was used in all castings. Figure 1a shows the schematic diagram of the wax mould cluster with trailing edge facing the central sprue. DS experiments were carried out using conventional Bridgman high rate solidification (HRS) technique in a vacuum environment. The ceramic mold temperature was 1500 °C in the experiments. The alloy of PWA 1483 was heated to 1550 °C and held at temperature for 5 minutes. The temperature was dropped to the casting temperature (1500 °C) and the melt was poured into the preheated mold. After 2-minutes of holding, to allow the system to attain a thermal equilibrium, the assembly was withdrawn at a constant rate of 3 mm/min. 60 castings (ten mould clusters with six castings in each cluster) were produced in the experiments.

### B. Macro and Microstructure Characterization

All SX castings were macro-etched using a solution consisting of HCl and H<sub>2</sub>O<sub>2</sub> (volume ratio 1:1) after removing the SX starter.

EBSD was applied to examine the orientation evolution of sliver. The casting was first cut by wire-based electrical discharge machining (EDM) along the growth direction of sliver (along line I in Figure 1(b)). Then a series of EBSD samples, 2 mm in thickness, were cut off along the dotted line in Figure 1(b). They were all mechanically ground, polished and electro-polished in a solution containing 10 pct HClO<sub>4</sub>-90 pct C<sub>2</sub>H<sub>5</sub>OH at room temperature with 10 V direct current and a soaking period of 10 s for EBSD experiments. All samples in one casting were placed on the EBSD specimen stage along cut I in order to maintain their relative position in the casting. A reference coordinate system was defined as shown in Figure 1(c) where [100] axis is parallel to cut I and [001] axis is the DS direction. EBSD mapping around sliver/matrix interface was conducted. All data collected from EBSD was processed by the Oxford HKL Channel 5 software to obtain the

**Table I. Nominal Composition of the Superalloy Used in the Experiments (in Wt Pct)**

Alloy	C	Cr	Co	W	Mo	Al	Ti	Ni
PWA 1483	0.05	12.0	9.0	4.0	2.0	3.4	4.0	Bal

orientation of sliver and matrix and the misorientation between them.

After that, these EBSD samples were chemically etched for optical microscope observation. In order to understand the dendrite branching of sliver and the formation of diverging or converging boundary between sliver and matrix during solidification, the samples were cut longitudinally along the secondary dendrite arm on the cross section to reveal the primary dendrite arms of both sliver and matrix. These samples were all mechanically ground, polished and etched in a solution of 4 g CuSO<sub>4</sub>, 10 ml HCl and 20 ml H<sub>2</sub>O. Microstructure was observed by optical metallographic microscope (OM-IMc 5).

### C. Numerical Simulation

The commercial software ProCAST (ESI Group, Paris) was applied to calculate the thermal and stress field during directional solidification. The numerical simulation was conducted based on the finite element (FE) method and basic heat transfer equations.

The main heat transfer processes during DS were determined by the heat conduction within the melt, heat transfer between melt and mold, heat conduction through mold and the radiation heat transfer among mold and cooling zone.<sup>[14]</sup> Table II shows the initial conditions, boundary conditions and the interface heat-transfer coefficients between different domains used in the simulation. Heat-transfer coefficient between mold and metal used to simulate the gap at the interface induced by solidification shrinkage was a temperature-dependent parameter. The thermophysical properties of superalloys for the FE-based simulation are listed in Table III. Thermal stress during solidification was calculated using the thermal and mechanical properties of PWA 1483 obtained from the software according to the alloy composition. Solidified metal, with isotropic hardening and elasto-plastic constitutive relation was assumed and creep deformation was ignored. Moreover, the ceramic mold was considered to be isotropic elastic and thus plastic deformation, creep and fracture were also ignored.

## III. RESULTS

### A. Macro and Microstructure Characterization of Sliver

In the experiments nine castings containing a sliver defect were found among 60 SX castings after macro etching. The different positions of the sliver in 9 castings were schematically shown in Figure 2. Four slivers were found on the pressure surface of the airfoil, while five observed on the suction side.

Figures 3(a) and (b) show the typical macro-morphology of sliver defect on the SX casting surface. The strip-like structure on matrix can be clearly observed. The slivers were about 0.5 mm in width at their initiation site. The width of most slivers remained constant (Figure 3(a)), while only one (sliver in casting 7) increased gradually during DS (Figure 3(b)). All

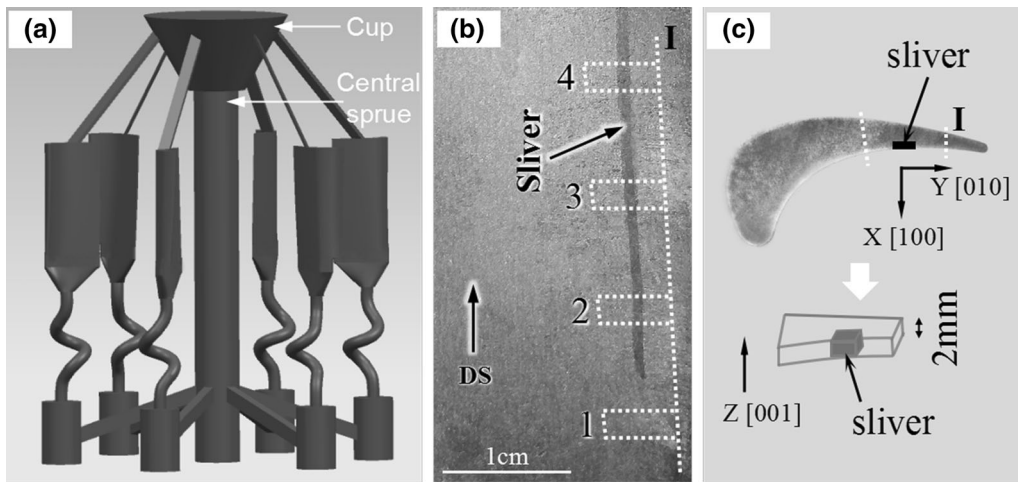


Fig. 1—Schematic diagrams of the (a) wax mould cluster and EBSD samples (b) sampling and (c) measurement.

**Table II. Model Parameters Used in the Simulation**

Parameters	Value
Initial Conditions (°C)	
Melting Temperature	1550
Pouring Temperature	1500
Chill-Plate Temperature	150
Boundary Conditions	
Temperature of Heating Zone	1500 °C
Emissivity of Heating Zone	0.8
Temperature of Cooling Zone	150 °C
Emissivity of Cooling Zone	0.8
Emissivity of Mold	0.4
Interface Heat-Transfer Coefficients	
Melt-Chill Plate	$1000 \text{ W (m}^2 \text{ K)}^{-1}$
Mold-Chill Plate	$50 \text{ W (m}^2 \text{ K)}^{-1}$
Mold-Melt	$0 \sim 750 \text{ W (m}^2 \text{ K)}^{-1}$

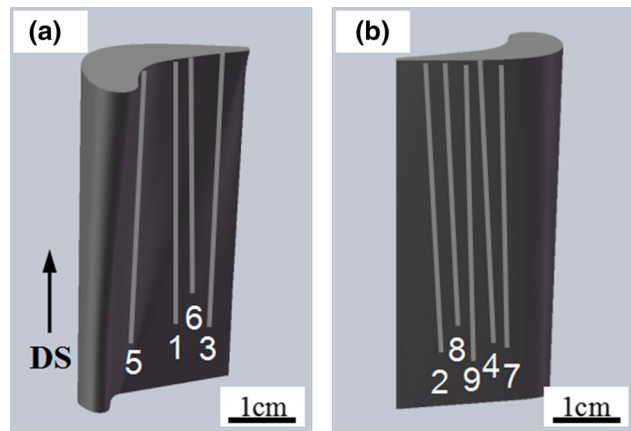


Fig. 2—Schematic illustration of slivers on (a) pressure and (b) suction surface of the castings.

**Table III. Thermophysical Properties of Superalloys Used in the Simulation<sup>[15]</sup>**

Parameters	Value
Liquidus Temperature	1354 °C
Solidus Temperature	1289 °C
Melting Range	65 °C
Heat Capacity	0.49 ~ 0.65 kJ/kg/°C
Thermal Conductivity	16 ~ 33 W/m/°C
Withdrawal Rate	3 mm/min

sliver defects extended along the DS direction to the top of the casting.

The orientation of sliver and matrix at position 2 (shown in Figure 1b) in 9 castings was compared in Table IV. Most slivers generated in castings that had relatively large deviation from DS direction ( $> 10$  deg). All slivers were tilt from matrix along the [001]. In most

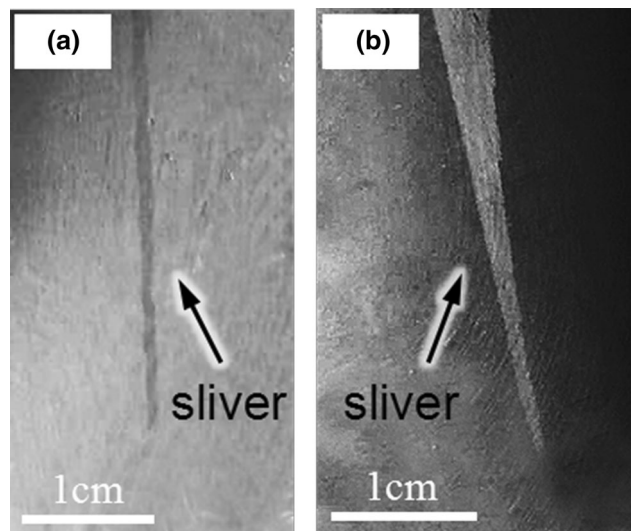


Fig. 3—Sliver defect observed in SX casting surface: (a) and (b) the typical macro-morphology.

casings (except 3 and 4), the sliver was inclined to DS direction by a smaller angle compared to that of the matrix and generally contained 1 to 2 primary dendrites (Figure 4(a)). It is also interesting to note that all of the slivers in 9 castings originated from a diverging boundary between the mold wall and matrix and 7 slivers formed another diverging boundary with matrix, as illustrated in Figure 4(b). Slivers in casting 3 and 4 exhibited a slightly higher deviation from DS direction compared with that of the matrix ( $\leq 2$  deg) and formed converging boundary with respect to matrix (Figure 4(c)).

Some of the slivers rotated relative to the matrix on the plane perpendicular to the DS direction, *i.e.*, the [100] and [010] orientation of the sliver and matrix was different in some castings. Figure 5 reveals two cases of the alignment of dendrites in the cross section. The secondary dendrite arms of sliver were either misaligned (Figure 5(a)) or parallel to that of the matrix (Figure 5(b)).

The misorientation between sliver and matrix was 3.5 to 9.8 deg (Table IV), which indicates that sliver was generally separate from the matrix by low angle grain boundaries. (Misorientation describes the orientation difference between two grains in terms of a rotation angle of their crystal coordinate systems into coincidence. The smallest rotation angle is defined as a misorientation.<sup>[16]</sup>)

### B. Orientation Evolution of Sliver

The EBSD results obtained along the sliver (positions 1 to 4 in Figure 1(b)) indicate that the sliver in most castings did not change the orientation during solidification (see casting 3 as an example), as shown in Table V. The misorientation between sliver and matrix remained constant during the whole DS process.

However, we did find that the [100] and [010] orientation of both sliver and matrix in one of the castings (casting 5) changed continuously during DS as shown in Table VI. Figure 6 shows the typical morphology on the cross section, 3D-crystal orientation figures and pole figures of sliver and matrix in this casting. It can be seen from 3D-crystal orientation and pole figures that the secondary dendrites of sliver and matrix were rotating clockwise around the [001] axis during directional solidification. It is interesting to see that the rotation was simultaneously. Whereas, the deviation from DS direction of both sliver and matrix, as well as the misorientation between sliver and matrix did not change.

### C. Dendrite Branching of Sliver

The typical optical micrographs in the cross section at positions 2 to 4 (Figure 1(b)) are shown in Figures 7(a) through (c) (pictures taken from casting 4). The sliver initiated from two deformed dendrites as shown in Figure 7(a). Sliver developed into the SX casting slowly during solidification (Figures 7(b) and (c)), *i.e.*, there was no extension on the casting surface, corresponding to the sliver with constant width in Figure 3(a).

However, the sliver in casting 7 expanded not only into the casting but also on the casting surface, and the width gradually increased on the casting surface as seen in Figures 7(d), (e) and 3(b). The deformed dendrites developed quickly. The width of this sliver at the initiation site was comparable to that of the other slivers (see Figure 3). Whilst, around 15 dendrites can be observed at position 3 (Figure 7(d)) and the misoriented area became very large at position 4 (Figure 7(e)). It is worth to note that the sliver in casting 7 exhibited large misorientation with respect to matrix on the cross section compared to other sliver defects according to Table IV and Figure 7.

Figure 8 shows the competitive growth between sliver and matrix on the longitudinal plane along the DS direction (picture taken from casting 7). Although some dendrites of better aligned sliver were occasionally blocked by the secondary arms of matrix (as marked by the arrow) during competitive growth, the sliver was able to overgrow matrix along the DS direction, and extended along the DS direction to the top of the casting.

## IV. DISCUSSION

### A. Orientation Evolution of Sliver

During DS most of the deformed dendrites grew in a rather stable pattern. The misorientation between the sliver and matrix, as well as the misorientation between sliver and DS direction remained unchanged throughout the whole solidification. However, there was one exceptional case observed in the present experiments as seen in Figure 6. The misorientation between sliver and matrix in casting 5 was unchanged throughout the DS process, but the secondary dendrite arms of sliver and matrix were rotating around the DS direction as solidification proceeded. This is probably related to the complex geometry of the casting. Careful observation of Figs. 1 and 2 shows that the sliver in casting 5 generated on the pressure surface near the leading edge of the casting where a large curvature exists from bottom to the top.

Large curvature may result in large stress. Figure 9 shows the effective stress contours on the different cross sections (bottom and top) calculated by ProCAST when the solid fraction was about 0.7, below which dendrite bridging did not establish and transmission of the stresses cannot be achieved.<sup>[11]</sup> A stress of 50–60 MPa was observed near the position of sliver 5, which was in the same order of magnitude comparing to the yield strength of the mushy zone as estimated in Reference 17. However, the stress level near all slivers was almost the same in Figure 9a. While in Figure 9(b), the stress level near sliver 5 was the lowest. Thus it can be deduced that contraction stress may have little effect on the rotation of dendrites.

The change of cross-sectional area along the DS direction of the casting can also cause the change of temperature gradient, leading to the deviation of growth direction.<sup>[18]</sup> Figure 10 exhibits the temperature gradient

**Table IV. EBSD Results at Position 2 (Fig. 1(b)) of 9 Castings with a Sliver**

Castings	Sliver (Deg)			Matrix (Deg)			Misorientation (Deg)
	[100]	[010]	[001]	[100]	[010]	[001]	
1	10.3	9.9	6.2	11.7	9.3	7.4	3.5
2	21.0	18.9	11.9	23.5	16.7	18.6	7.0
3	8.9	13.8	12.3	6.2	10.6	10.6	3.5
4	32.2	34.0	12.1	26.8	29.2	10.1	6.2
5	17.3	17.9	9.2	25.9	25.1	10.8	8.5
6	17.0	18.4	10.0	14.0	15.1	11.9	3.8
7	30.3	30.8	6.6	19.7	16.4	11.4	9.8
8	37.8	40.3	14.0	36.6	41.2	19.3	7.3
9	20.5	20.9	4.5	18.8	19.2	12.1	7.5

The reference coordinate system is shown in Fig. 1(c).

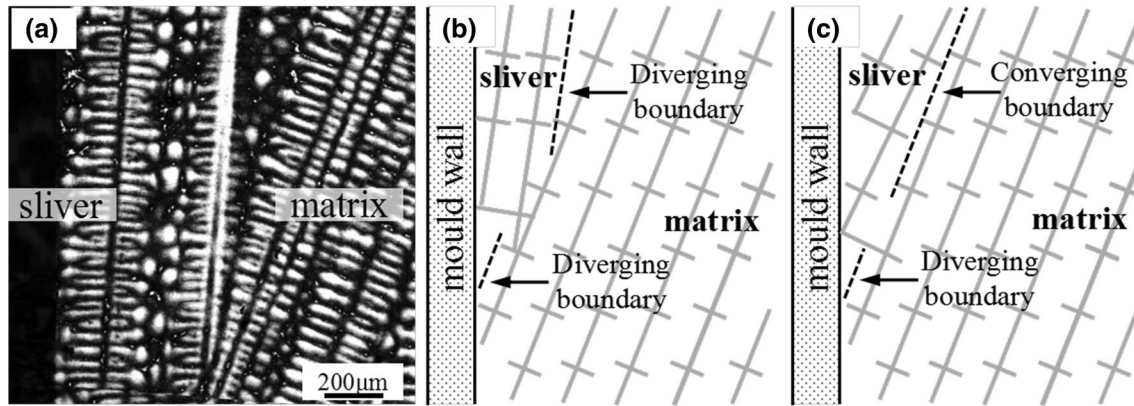


Fig. 4—(a) Longitudinal section micrograph, and schematic illustration of the (b) diverging and (c) converging boundary between sliver and matrix.

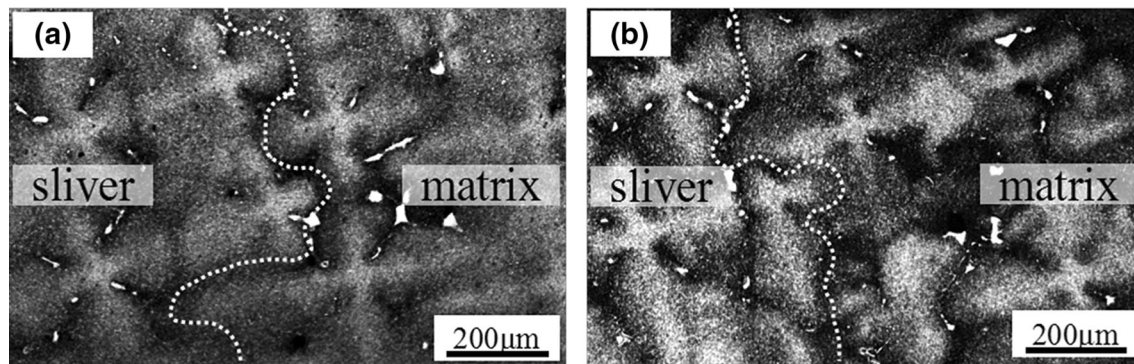


Fig. 5—Cross section micrograph showing the secondary dendrite arms of sliver (a) misaligned and (b) parallel to that of the matrix.

**Table V. Orientation Evolution of Sliver and Matrix in Casting 3 Along DS Direction**

Positions	Sliver (Deg)			Matrix (Deg)			Misorientation (Deg)
	[100]	[010]	[001]	[100]	[010]	[001]	
4	7.8	13.3	12.7	5.3	10.1	10.1	3.8
3	8.6	12.7	11.0	6.0	9.3	8.5	3.8
2	8.9	13.8	12.3	6.2	10.6	10.6	3.5
1	—	—	—	6.0	10.2	11.0	—

on the cross section (temperature gradient on plane XY) at the bottom and top of the casting. The approximate directions of thermal convection on the cross section were marked by arrows. It is obvious that the thermal convection direction around sliver 5 varied significantly from bottom (MN) to the top (M'N') of the casting compared to that of the other slivers (see the direction of thermal convection near sliver 6 as an example). It is believed that the change of thermal convection in the limited growth space promoted the rotation of secondary arms of sliver and matrix. In the mushy zone, the enriched solute and heat around the dendrite tips were transported timely by the thermal convection. Thus the lower temperature and less solute existed in the upstream melt, which was beneficial for the dendrite growth. Subsequently, the secondary dendrite arms grew towards the upstream direction, thereby producing the clockwise rotation observed in Figure 6.

### B. Dendrite Branching of Sliver

The competitive growth behavior of two neighbouring dendrites has been related to the solute field in interdendritic area.<sup>[19]</sup> The Péclet number of solute diffusion  $P_c$  (associated with the driving force of solute diffusion at dendrite tip) is determined by Eq. [1]<sup>[20]</sup>:

$$P_c = VR/2D = R/\delta_c \quad [1]$$

where  $V$  is withdrawal speed,  $R$  is the radius of dendrite tip,  $D$  is diffusion coefficient and  $\delta_c$  is the solute field range.

Solute field range  $\delta_c$  is used to describe the thickness of solute diffusion layer in front of the dendrite tip during DS.  $\delta_c$  is dominated by withdrawal speed  $V$  and diffusion coefficient  $D$  according to Eq. [1], and written as:

$$\delta_c = 2D/V \quad [2]$$

If the space between two neighbouring dendrite tips decreases to the point where the two solute fields encounter, solute interaction occurs and the growing of dendrites ceases, *i.e.*, the stronger the solute interaction, the weaker the branching effect.<sup>[20,21]</sup>

There was little extension of sliver on the casting surface in most castings, *i.e.* sliver only extended into the casting slowly during solidification (Figures 7(a) through (c)). Whereas only one sliver in casting 7 extended on the casting surface and into the casting quickly (Figures 7(d) and (e)). It seems that this branching behavior after formation of sliver defects is primarily related to the misorientation on the cross section perpendicular to the DS direction. Large misorientation resulted in quick branching as shown in Figures 7(d), (e). According to Eq. [2], a solute field range  $\delta_c$  of  $\sim 60 \mu\text{m}$  is estimated in front of the dendrite tip in the present experiments. It is obvious that the large misorientation between sliver and matrix on the cross section in casting 7 increased the distance (about  $126 \mu\text{m}$ ) between the secondary dendrite tips of sliver and matrix, which resulted in a weaker solute

interaction. Moreover, large misorientation between the secondary arms also provide more space for the dendrite branching. As a result, the dendrite branching at sliver/matrix interface was therefore promoted. The width of this sliver on the casting surface gradually increased and the dendrites extended into the casting quickly throughout the directional solidification. As for other slivers, the close distance of neighbouring dendrite tips and strong solute interaction weakened the dendrite branching effect.

In most castings, sliver was inclined to DS direction by a smaller angle than matrix, *i.e.*, sliver formed diverging boundary with matrix as shown in Figure 4(b) and Table IV. It is occasional to see that the tertiary branches generated from favorite oriented sliver were blocked by surrounding side branch of the matrix (Figure 8). It is reported that this stochasticity of the occurrence of such blocking is related to the coarser side branch, which also contributes to the fluctuation of new tertiary branches generation from the well-aligned grain.<sup>[22]</sup> Still, the dendrite development of well-aligned sliver can lead to the incline of grain boundary (GB) from sliver to matrix and reducing of growth space of matrix. Finally, the misaligned matrix can be gradually overgrown by the well-aligned sliver with the solidification according to the literatures.<sup>[19,23 through 25]</sup>

In the case of converging boundary between sliver and matrix (Figure 4(c)) in casting 3 and 4, the sliver was unfavorably oriented compared to that of the matrix, but not overgrown by matrix. It is highly likely that neither sliver nor matrix occupies the advantage during the competitive growth along the DS direction due to the very small misorientation between [001] axes of them ( $\leq 2$  deg). The similar pattern of overgrowth between bi-crystal at converging boundary under the condition of small misorientation between [001] axes of the bi-crystal (within 5 deg) was also reported by Tourret *et al.*<sup>[26]</sup>

Based on the analysis above, two manners of dendrite branching of sliver during DS are obtained, as illustrated in Figure 11. All slivers can extend along the DS direction to the top of the casting. In most castings, the misorientation between the secondary arms of sliver and matrix is small. Slivers do not extend on the casting surface and only grow into the casting slowly, as shown in Figure 11(a). On the other hand, in Figure 11(b), sliver can extend on the casting surface and into the casting quickly when the misorientation is large.

It is worthy to note that the statistical result of all 9 castings showing sliver defects revealed that the deviation angle from casting axis of 8 castings was between 10.1 and 19.3 deg and there was only one with a deviation below 10 deg (7.4 deg), as shown in Table IV. These results verified that the sliver would occur more easily in the casting with a larger deviation from casting axis. Thus a better aligned [001] axis of the dendrites with less branching will have low possibility to generate slivers, *i.e.* any optimization that can reduce the deviation from DS direction are useful strategies to avoid sliver.

**Table VI. Orientation Evolution of Sliver and Matrix in Casting 5 along DS Direction**

Positions	Sliver (Deg)			Matrix (Deg)			Misorientation (Deg)
	[100]	[010]	[001]	[100]	[010]	[001]	
4	20.7	22.0	9.6	28.7	28.3	10.6	8.6
3	18.2	18.8	8.4	26.5	26.0	9.6	9.1
2	17.3	17.9	9.2	25.9	25.1	10.8	8.5
1	—	—	—	21.7	20.8	8.9	—

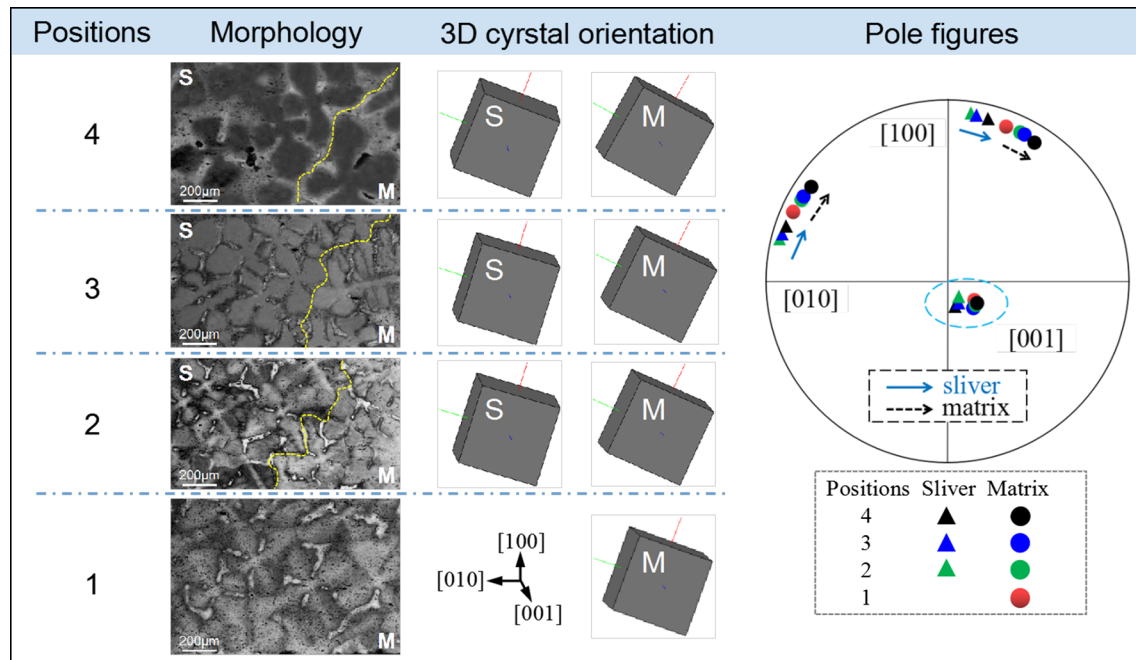


Fig. 6—Orientation evolution of sliver and matrix in casting 5 along DS direction. S is sliver and M stands for matrix.

## V. SUMMARY

The orientation evolution and dendrite branching of sliver defect after formation in a Ni-based single crystal superalloy have been studied in this work. Following major conclusions can be drawn:

1. Sliver generally initiated from 1 to 2 tertiary dendrites at the diverging boundary between the mould wall and matrix. All slivers were tilt from matrix along the [001] and most slivers were inclined to DS direction by a smaller angle compared to that of the matrix. Some of slivers rotated relative to the matrix on the plane perpendicular to the DS direction. The overall misorientation between the sliver and matrix was low, between 3.5 and 9.8 deg in the present study.
2. Slivers observed in SX castings generally grew with a fixed orientation throughout the DS process. However, the orientation of the secondary dendrite

arms of both sliver and matrix could change simultaneously probably as a result of the geometry constraint of the casting. Compared to the contraction stress, thermal convection played an important role in the rotation of secondary dendrite arms of sliver and matrix.

3. All slivers were able to overgrow matrix on the longitudinal section along the DS direction and extended into the casting during solidification. In castings where the misorientation between secondary dendrite arms of sliver and matrix was small, slivers did not extend on the casting surface and the width of them did not change from bottom to top. However, if the misorientation on the cross section was large, sliver extended on the casting surface and into the casting quickly. Such different manners of dendrite branching can be attributed to the interaction of solute field in the interdendritic area.

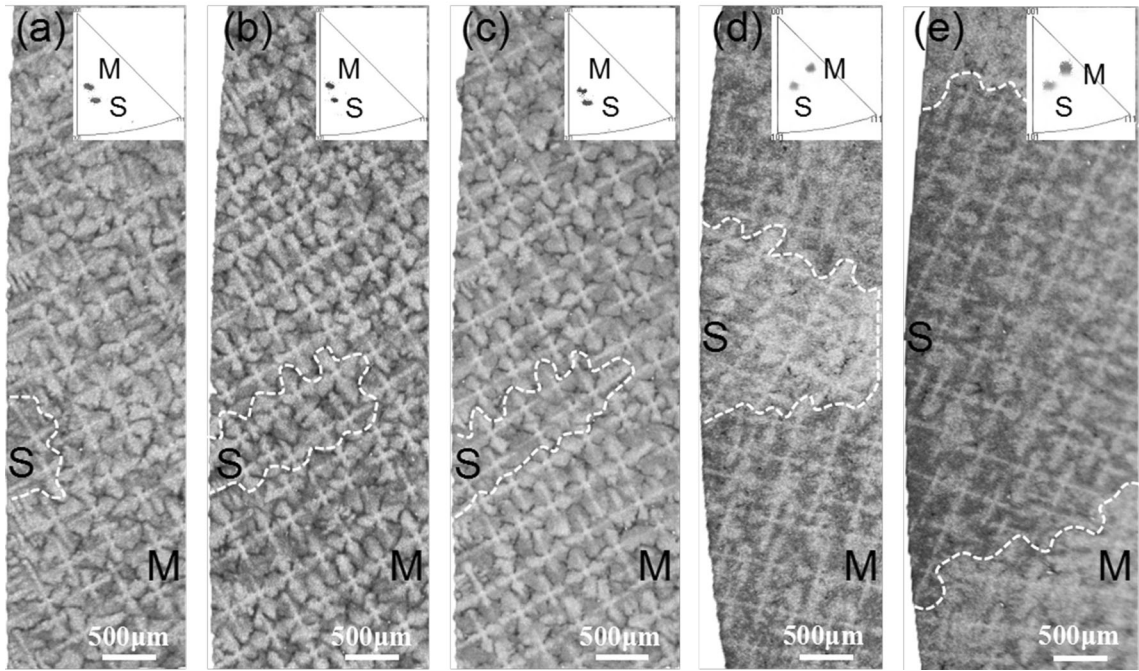


Fig. 7—Typical optical micrograph of (a) through (c) sliver at positions 2 to 4, and (d) and (e) sliver in casting 7 at positions 3 and 4 indicated in Fig. 1b. Surface to the left is the casting surface and the right side is the casting centre. The insets in the up right corner are inverse pole figures map corresponding to  $X$ -axis. The sliver defects (S) are marked out with dash lines from matrix (M).

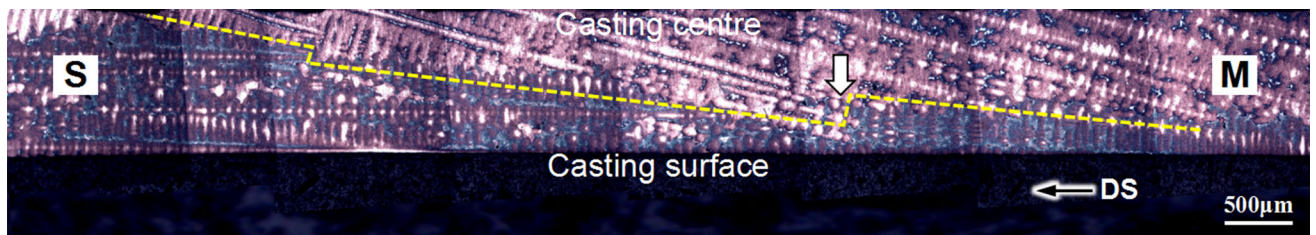


Fig. 8—Optical micrograph showing the competitive growth between sliver and matrix on the longitudinal plane along the DS direction. The sliver (S) is marked out with dash line from matrix (M).

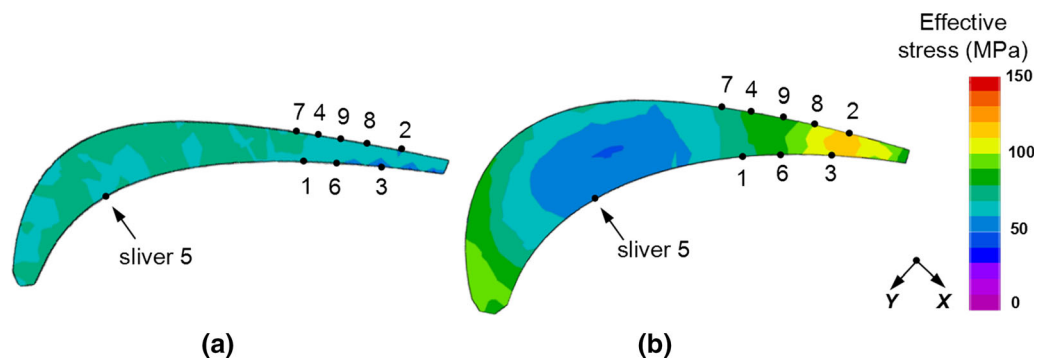


Fig. 9—Stress contours on the cross section at the (a) bottom and (b) top of the casting calculated by ProCAST. Position of 9 slivers is labeled.



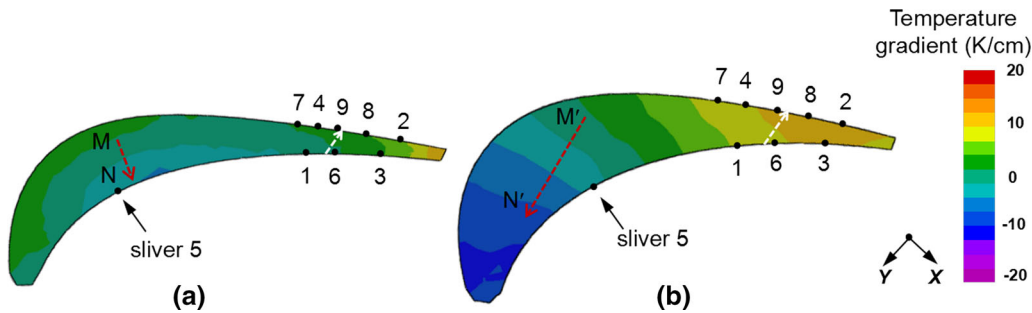


Fig. 10—Temperature gradient on the cross section at the (a) bottom and (b) top of the casting calculated by ProCAST. Position of 9 slivers is labeled. Arrows indicate the thermal convection on the cross section.

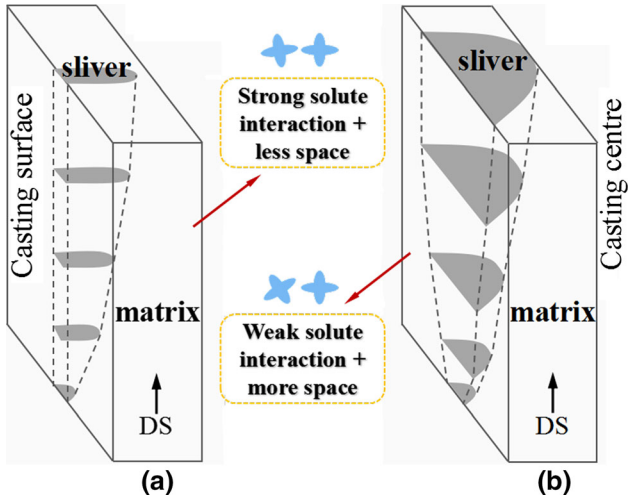


Fig. 11—Schematic illustration of the dendrite branching of sliver after formation. (a and b) are respectively corresponding to the sliver in Figs. 3(a), (b). The sliver is marked out with dashed lines from matrix.

## ACKNOWLEDGMENTS

This work was financially supported by the National Key Research and Development Program of China (Grant No. 2016YFB0701403), National Natural Science Foundation of China (Grant Nos. 51631008, 91860201, 51771204 and U1732131), National Science and Technology Major Project (Grant Nos. 2017-VII-0008-0101 and 2017-VI-0003-0073) and Key Deployment Projects of the Chinese Academy of Sciences (Grant No. ZDRW-CN-2019-01). The authors are grateful for those supports.

## REFERENCES

1. R.C. Reed: *The Superalloys: Fundamentals and Applications*, Cambridge University Press, Cambridge, 2006.
2. T.M. Pollock and S. Tin: *J. Propul. Power*, 2006, vol. 22, pp. 361–74.
3. N. Stanford, A. Djakovic, B.A. Shollock, M. McLean, N. D'Souza, and P.A. Jennings: *Scr. Mater.*, 2004, vol. 50, pp. 159–63.

4. N. D'Souza, P.A. Jennings, X.L. Yang, H.B. Dong, P.D. Lee, and M. McLean: *Metall. Mater. Trans.*, 2005, vol. 36B, pp. 657–66.
5. S. Tin, T.M. Pollock, and W. Murphy: *Metall. Mater. Trans. A*, 2001, vol. 32, pp. 1743–53.
6. D.Y. Han, W.G. Jiang, J.H. Xiao, K.W. Li, Y.Z. Lu, W. Zheng, S.H. Zhang, and L.H. Lou: *J. Alloy Compd.*, 2019, vol. 805, pp. 218–28.
7. A. Morawiec: *Scr. Mater.*, 2009, vol. 61, pp. 438–40.
8. Y. Wang, D. Wang, G. Zhang, L.H. Lou, and J. Zhang: *Superalloys 2016*, TMS, Warrendale, 2016, pp. 757–62.
9. D.J. Sun, L. Liu, T.W. Huang, W.C. Yang, C. He, Z.R. Li, J. Zhang, and H.Z. Fu: *Metall. Mater. Trans. A*, 2019, vol. 50A, pp. 1119–24.
10. J.W. Aveson, P.A. Tennant, B.J. Foss, B.A. Shollock, H.J. Stone, and N. D'Souza: *Acta Mater.*, 2013, vol. 61, pp. 5162–71.
11. Y.Q. Huang, J. Shen, D. Wang, G. Xie, Y.Z. Lu, L.H. Lou, and J. Zhang: *Metall. Mater. Trans. A*, 2020, vol. 51, pp. 99–103.
12. J.R. Li, J.Q. Zhao, S.Z. Liu, and M. Han: *Superalloys 2008*, TMS, Warrendale, 2008, pp. 443–51.
13. J.C. Stinville, K. Gallup, and T.M. Pollock: *Metall. Mater. Trans. A*, 2015, vol. 46, pp. 2516–29.
14. Y.F. Li, L. Liu, D.J. Sun, Q.Z. Yue, T.W. Huang, B. Gan, J. Zhang, and H.Z. Fu: *J. Alloy Compd.*, 2019, vol. 773, pp. 432–42.
15. Y.Z. Lu, J. Shen, W. Zheng, Z.G. Xu, G. Zhang, and G. Xie: *J. Mater. Eng.*, 2016, vol. 44, pp. 1–8.
16. P. Yang: *Electron Backscattered Diffraction Technique and Applications*, Metallurgical Industry Press, Beijing, 2007.
17. C. Panwisawas, H. Mathur, J.-C. Gebelin, D. Putman, C.M.F. Rae, and R.C. Reed: *Acta Mater.*, 2013, vol. 61, pp. 51–56.
18. M.L. Clemens, A.R. Price, and R.S. Bellows: *Advanced Materials and Processes for Gas Turbines* (2003), pp. 111–18.
19. Y.Z. Zhou, A. Volek, and N.R. Green: *Acta Mater.*, 2008, vol. 56, pp. 2631–37.
20. W. Kurz and D.J. Fisher: *Fundamentals of Solidification*, Trans Tech Publications, Aedermannsdorf, 1984.
21. Y.Z. Zhou and X.F. Sun: *Sci. China Tech. Sci.*, 2012, vol. 55, pp. 1327–34.
22. C.W. Guo, J.J. Li, H.L. Yu, Z.J. Wang, X. Lin, and J.C. Wang: *Acta Mater.*, 2017, vol. 136, pp. 148–63.
23. D. Walton and B. Chalmers: *Trans. Metall. Soc. AIME*, 1959, vol. 215, pp. 447–57.
24. C.A. Gandin and M. Rappaz: *Acta Metall. Mater.*, 1994, vol. 42, pp. 2233–46.
25. M. Rappaz, C.A. Gandin, J.L. Desbiolles, and P. Thévoz: *Metall. Mater. Trans. A*, 1996, vol. 27A, pp. 695–705.
26. D. Tourret, Y. Song, A.J. Clarke, and A. Karma: *Acta Mater.*, 2017, vol. 122, pp. 220–35.

**Publisher's Note** Springer Nature remains neutral with regard to jurisdictional claims in published maps and institutional affiliations.